International Journal of Hydrogen Energy 169 (2025) 151031

Contents lists available at ScienceDirect

International Journal of Hydrogen Energy

journal homepage: www.elsevier.com/locate/he

0D/3D $ZnIn_2S_4/NiCo_2O_4$ heterojunction for efficient visible light hydrogen production

Xulong Sun [a,c,1], Yongping Luo [b,1], Yong Chen [c,1], Yuhua Dai [c], Yu Xie [c,*], Yuxiu Wang [a,**], Jiansheng Zhang [d,***]

[a] Key Laboratory of Nanchang City for Green New Materials and Industrial Wastewater Treatment, School of Ecology and Environment, Yuzhang Normal University, Nanchang, 330103, China
[b] Huzhou Key Laboratory of Green Energy Materials and Battery Cascade Utilization, School of Intelligent Manufacturing, Huzhou College, Huzhou, 313000, China
[c] College of Environment and Chemical Engineering, Nanchang Hangkong University, Nanchang, 330063, China
[d] Department of Energy and Power Engineering, Tsinghua University, Beijing, 100084, China

ARTICLE INFO

Handling Editor: Dr M Mahdi Najafpour

Keywords:
$ZnIn_2S_4$
$NiCo_2O_4$
Hetrojunction
Photocatalytic hydrogen production

ABSTRACT

The exceptional photocatalytic H_2 production capacity of metal sulfides has garnered considerable attention within the scientific community. However, the issue of photocorrosion represents a significant obstacle to their industrial deployment. Consequently, the prevention of photocorrosion represents a pivotal challenge for the industrial deployment of metal sulfide catalysts. In this study, the synthesis of $ZnIn_2S_4/NiCo_2O_4$ catalysts was successfully completed, and they exhibited satisfactory hydrogen evolution performance. The incorporation of 7 % $NiCo_2O_4$ into the catalyst led to a noteworthy maximum photocatalytic H_2 generation rate of 4.73 μmol h^{-1} g^{-1}, which exhibited a considerable 4.11-fold improvement in performance compared to that of pure $ZnIn_2S_4$. The high photocatalytic activity was maintained throughout four experimental cycles. The findings suggest that the heterostructure formed by $ZnIn_2S_4$ and $NiCo_2O_4$ enhances the separation efficiency of photogenerated electron-hole pairs and improves the H_2 generation capacity and stability of the catalyst. This $ZnIn_2S_4/NiCo_2O_4$ composite photocatalyst exhibits a high response to visible light, superior photochemical stability, and a broad range of applications in solar photocatalytic hydrogen production from water decomposition.

1. Introduction

Fossil fuels are the foundation of contemporary industry, however, their utilisation has resulted in environmental concerns, including air pollution and the greenhouse effect, which present a significant risk to human health [1–3]. Concurrently, the finite nature of fossil fuel reserves presents a challenge in meeting the increasing demand for energy [4]. It is therefore imperative to identify an environmentally friendly and sufficient new energy source to replace conventional fuels [5]. Hydrogen (H_2) has been the subject of considerable interest as a potential alternative fuel source, due to its high energy density and environmentally friendly properties [6,7]. The photocatalytic hydrolysis of hydrogen has been the subject of considerable interest as a means of directly converting solar energy into chemical energy [8]. However, these materials present a number of challenges, including low solar energy utilisation efficiency, complex preparation, photocorrosion and poor catalyst stability [9–13]. It is therefore imperative to develop efficient, stable and cost-effective photocatalysts in order to facilitate the advancement of photocatalytic hydrogen production technology [14].

$ZnIn_2S_4$ (ZIS) has been the subject of considerable interest as a novel AB_2S_4 ternary sulfide photocatalyst, largely due to its narrow band gap of 2.1–2.4 eV and its excellent photocatalytic performance [15,16]. Early studies have demonstrated that ZIS exhibits remarkable catalytic activity in the production of hydrogen by photocatalysis and the degradation of organic pollutants [17,18]. However, due to the strong reducing nature of S^{2-} ions, they are susceptible to photocorrosion triggered by the oxidation of photogenerated holes, which has the effect

* Corresponding author.
** Corresponding author.
*** Corresponding author.
E-mail addresses: xieyu_121@163.com (Y. Xie), wangyuxiu@yuznu.edu.cn (Y. Wang), zhang-jsh@tsinghua.edu.cn (J. Zhang).
[1] They have contributed equally to this work.

https://doi.org/10.1016/j.ijhydene.2025.151031
Received 10 May 2025; Received in revised form 11 August 2025; Accepted 16 August 2025
Available online 27 August 2025

of weakening the stability of the catalyst [19]. Furthermore, the pure ZIS catalyst exhibits a high electron-hole recombination rate, which constrains the efficiency of hydrogen production [20]. In order to overcome these challenges, the researchers put forward a number of strategies designed to facilitate the separation of charge carriers in ZIS. These included changes to the morphology and surface structure of the material, as well as the introduction of noble metals as co-catalysts, with the aim of enhancing its photocatalytic hydrogen production performance [21–23]. Meanwhile, transition metal doping and structural engineering technologies have been extensively applied in the optimization of photocatalysts. Taking MOF-derived materials as an example [14], their layered structures significantly enhance light absorption efficiency and charge transfer performance. These techniques can also be utilized to overcome the limitations of ZIS catalysts.

It is observed that the construction of heterojunction composites not only preserves the characteristics of each component, but also facilitates electron transfer and encourages the separation of photo-induced electron-hole pairs [24–26]. This results in the creation of additional active sites for the reduction half-reaction on the surface of the photocatalyst, which consequently enhances its catalytic performance [27]. Recent research advances have further validated the potential that heterojunction materials developed through various strategies have demonstrated significant activity enhancements. For example, grain boundary-rich heterojunctions (Cu–ZnS/ZnCdS, 2920 μmol g^{-1} h^{-1}), lattice-coherent heterojunctions (Te/In_2O_3@MXene, 568.8 μmol g^{-1} h^{-1}), synergistic doping-vacancy coupled heterojunctions (Cu/S–In$(OH)_3$, 1.22 mmol g^{-1} h^{-1}), and core-shell Z-scheme heterojunctions (Ni–ZnO@C/g-C_3N_4, 336 μmol g^{-1} h^{-1}). These strategies provide valuable references for designing high-performance heterostructured systems [28–31]. $NiCo_2O_4$ (NCO) is gaining increasing attention in the field of photocatalytic hydrogen production due to its significant redox capacity, high electrical conductivity, and appropriate conduction band position [32,33]. Initially, NCO can form heterojunctions with various semiconductors to enhance the efficiency of carrier separation, examples include $NiCo_2O_4$/$Zn_{0.1}Cd_{0.9}S$ and g-C_3N_4/$NiCo_2O_4$ [34,35]. Additionally, researchers such as Wang have repeatedly discussed the use of $NiCo_2O_4$-modified g-C_3N_4 for photocatalytic hydrogen production [36]. The presence of multivalent nickel and cobalt ions in these composites offers more active sites and improved electrical properties [37,38]. These collective findings highlight the promising potential of NCO in the realm of photocatalytic hydrogen production.

This study introduces a novel catalyst, ZIS/NCO, demonstrating outstanding performance in photocatalytic hydrogen evolution. To our knowledge, this is the first documented utilisation of ZIS/NCO catalysts for photocatalytic hydrogen production. When exposed to visible light, the composite's photocatalytic hydrogen production efficiency reached 4.7 μmol h^{-1} g^{-1}, marking a notable enhancement compared to pure ZIS, a 4.11-fold increase. Notably, the ZIS/NCO catalysts outperformed similar AB_2S_4 counterparts. The impact of $NiCo_2O_4$ incorporation on the structure and efficacy of ZIS/NCO photocatalysts was assessed through XRD, SEM, TEM, XPS, DRS, and photoelectrochemical analyses, offering a new avenue for designing high-performance AB_2S_4 photocatalysts and their application in photocatalytic hydrogen production.

2. Experimental

2.1. Materials

Zinc chloride ($ZnCl_2$), Indium nitrate tetrahydrate ($In(NO_3)_3{\cdot}4H_2O$), thioacetamide (C_2H_5NS), Nickel chloride hexahydrate ($NiCl_2{\cdot}6H_2O$), Cobalt chloride hexahydrate ($CoCl_2{\cdot}6H_2O$) were purchased from Shanghai Macklin biochemical technology Co., Ltd. ammonium bicarbonate (NH_4HCO_3), ethanol (C_2H_5OH), triethanolamine ($C_6H_{15}NO_3$) were purchased from Sinopharm Chemical Reagent Co., Ltd. All chemicals were obtained from commercial sources in analytical reagent (AR) grade without further purification.

2.2. Synthesis of ZIS

The synthesis was conducted using a hydrothermal method. Specifically, ZIS microspheres were prepared by dissolving $ZnCl_2$ (0.5 mmol), $InCl_3{\cdot}H_2O$ (1.0 mmol), and thioacetamide (TAA) (2.0 mmol) in 60 ml of deionized water. The mixture was stirred at 25 °C for 1 h before being transferred to an 100 ml Teflon-lined stainless steel autoclave. Subsequently, the solution was heated at 160 °C for 12 h. Following natural cooling to room temperature, a light yellow precipitate was obtained. The precipitate was then collected, washed several times with deionized water and ethanol, and finally dried at 80 °C for 12 h to facilitate further characterization.

2.3. Synthesis of NCO

In a 100 ml ethanol solution, 1 mmol $NiCl_2{\cdot}6H_2O$ and 2 mmol $CoCl_2{\cdot}6H_2O$ were combined. Then 10 mmol NH_4HCO_3 was added to the suspension. The mixture was stirred for 8 h, then centrifuged, washed with ethanol and dried at 80 °C for 12 h. The resulting composite was calcined in a muffle furnace at a heating rate of 5 °C min^{-1} to 400 °C for 2 h, yielding NCO.

2.4. Synthesis of ZIS/NCO

ZIS/NCO composite catalysts were prepared by electrostatic self-assembly. Initially, 200 mg of ZIS powder was measured and combined with 20 ml of ethanol in a beaker. The mixture was then sonicated to ensure uniform dispersion. A defined amount of NCO powder was then weighed and added to the solution, which was sonicated again. After sonication, the solution was stirred vigorously at 1000 rpm for 24 h. The resulting precipitate was collected and vacuum dried at 60 °C. After drying, the precipitate was ground into a powder to obtain an x% ZIS/NCO sample, where x is the mass percentage of NCO. The preparation process of ZIS/NCO composite material, as shown in Fig. 1, is translated as follows.

2.5. Characterization of catalysts

The phase composition of the sample was analyzed using XPS and XRD techniques, specifically the Axis Ultra DLD for XPS and the BRUKER instrument with Cu K-Alpha = 1.5408 for XRD. In addition, the shapes and structures of different photocatalysts were observed by TEM imaging with the FEI Talos F200X and SEM imaging with the FEI Quanta 250. To investigate carrier recombination rates and optical properties, PL measurements were performed using the Hitachi 7000 and DRS analysis was performed using the T9S spectrophotometer. The electrochemical evaluation involved a three-electrode system and included Mott-Schottky (M-S) analysis, photocurrent transient (I-T) measurements and electrochemical impedance spectroscopy (EIS).

2.6. Photocatalytic test

10 mg of catalyst was placed into a sealed quartz tube, followed by the addition of 9 ml of deionized water and 1 ml of triethanolamine (TEOA). The quartz tube was purged with argon gas for 30 min to eliminate all traces of air. A 300 W xenon lamp (CEL-HXF300-T3) equipped with a 380 nm filter was employed as the light source for the reaction, with a light intensity averaging 35.5 mW cm^{2-}. The experiment was carried out at room temperature. After 2 h of exposure to light, all generated gaseous products were collected. These products and their concentrations were analyzed utilising a gas chromatograph (Panna A91 Plus GC) with a thermal conductivity detector. In order to evaluate the stability of the photocatalytic hydrogen precipitation rate of the material, the ZIS/NTO-7 material was selected for cyclic testing of its hydrogen precipitation rate. Each cycle was maintained for a duration of 2 h. The cyclic experiments were carried out in four groups.

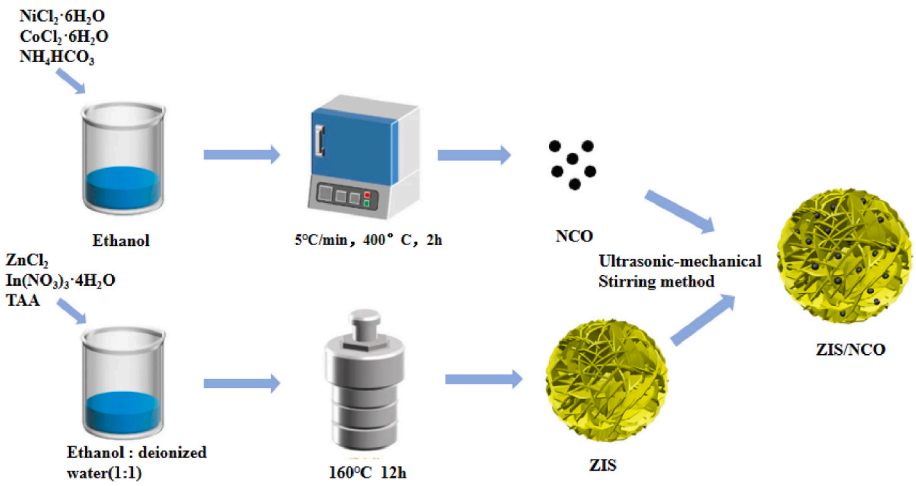

Fig. 1. The synthesis process of ZIS/NCO materials.

3. Result and discussion

The crystal structure information of the photocatalysts was verified by XRD patterns (Fig. 2). The XRD patterns of ZIS and NCO exhibited characteristic peaks corresponding to distinct crystal planes. In the case of ZIS, the diffraction peaks were particularly prominent at 21.4°, 27.2°, and 47.4°, which corresponded to the (006), (102), and (110) crystal planes, respectively (JCPDS No.65-2023) [39]. In NCO, the characteristic peaks at 18.74°, 36.71°, 44.73°, and 64.93° corresponded to the (111), (220), (311), and (220) crystal planes, respectively. (220), (311), and (440) crystal faces (JCPDS 20–0781) [40]. In the composites resulting from the combination of NCO and ZIS. First, the XRD patterns of the composite revealed distinct ZIS diffraction peaks at 21.4° (006), 27.2° (102), and 47.4° (110) (consistent with the JCPDS NO.65-2023 standard card). This indicates that ZIS maintained its crystalline structure intact after composite formation, serving as the primary framework of the heterostructure. Second, although the characteristic peaks corresponding to NCO were relatively weak in the composite, a faint signal was still detectable at 36.71° (corresponding to the (220) crystal plane of NCO, JCPDS NO.20-0781). This weak signal is attributed to the low NCO content in the composite material, confirming that NCO has been directly loaded onto the ZIS matrix. Third, no new diffraction peaks unrelated to ZIS or NCO appeared in the XRD patterns of the composite, excluding the formation of unintended by-products or impurities. This demonstrates that the ZIS/NCO bonding represents a pure composite process rather than a chemical reaction generating new phases. Fourth, compared with pure ZIS, the characteristic peaks of ZIS in the composite showed slight broadening (though not quantitatively determined). This phenomenon can be attributed to the intimate contact between ZIS and NCO, where interfacial interactions may induce local lattice distortion or grain size reduction in ZIS, further confirming their strong coupling relationship rather than simple physical mixing. In summary, the presence of ZIS-dominated peaks, identifiable trace NCO signals, absence of impurities, and interface-induced peak evolution collectively confirm the successful formation of the ZIS/NCO composite heterostructure.

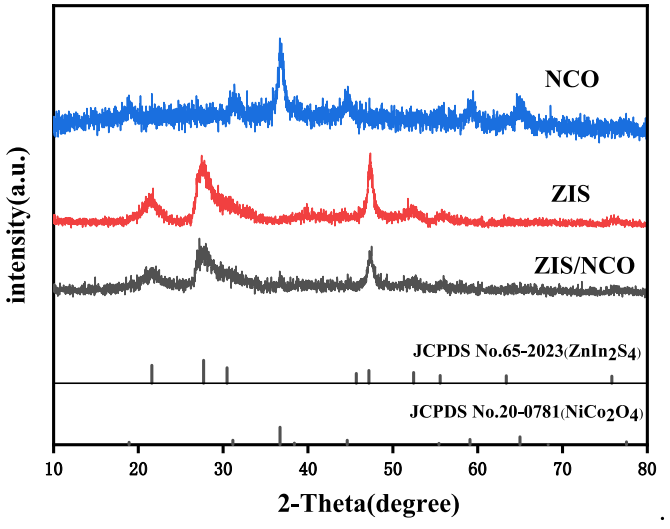

Fig. 2. XRD patterns of ZIS, NCO, and ZIS/NCO.

The external morphology and detailed structure of the catalyst were characterised by scanning electron microscopy and transmission electron microscopy analyses, respectively. Fig. 3a depicts NCO in its bulk form, comprising a multitude of nanoparticles. In contrast, Fig. 3b illustrates the three-dimensional flower-like spherical structure of ZIS, composed of nanosheets. As can be observed in the SEM image of ZIS/NCO in Fig. 3c, the granular NCO is attached to the surface of the ZIS flower-like sphere. To gain further insight into the microstructure of ZIS/NCO, the TEM images of ZIS/NCO in Fig. 3d–e are presented. These images are in agreement with the results observed in the SEM images. The high-resolution transmission electron microscopy (HRTEM) images (Fig. 3f) demonstrate that the lattice spacing of NCO is 0.205 nm, corresponding to the (311) crystallographic plane, and that the lattice spacing of ZIS is 0.321 nm, corresponding to the (102) crystallographic plane. These observations confirm the successful formation of a heterojunction. Furthermore, the elemental distribution map (Fig. 3g) demonstrating that sulfur, indium, zinc, oxygen, cobalt and nickel coexist and are uniformly distributed in the binary composites, thereby providing additional confirmation of the formation of the heterojunction.

The composition and surface chemical state of the samples were subjected to comprehensive investigation through the use of X-ray photoelectron spectroscopy (XPS) analysis. Fig. S1 illustrates the XPS investigation spectra of the ZIS/NCO composite, comprising S 2p, In 3d, Zn 2p, Ni 2p, Co 2p, and O 1s peaks. These spectra confirm the successful preparation of the composite. Fig. 4a illustrates the presence of two distinct peaks, with energies of 161.52 eV and 162.73 eV, respectively. These peaks can be attributed to the $s2p_{3/2}$ and $s2p_{1/2}$ orbitals of S^{2-}. Meanwhile, Fig. 4b illustrates that the signals at 444.87 eV and 452.41 eV originate from In $3d_{3/2}$ and In $3d_{5/2}$ of In^{3+}. With regard to Zn^{2+}, the binding energies of the $2p_{3/2}$ and $2p_{1/2}$ orbitals were found to be 1022.1 eV and 1045.18 eV, respectively, as illustrated in Fig. 4c. In Fig. 3d, the peaks at 854.63 eV (Ni $2p_{3/2}$) and 871.80 eV (Ni $2p_{1/2}$) are classified as Ni^{2+} chemical states, consistent with the bonding characteristics of typical nickel-based doped composites. Satellite peaks (Sat.) at 856.42

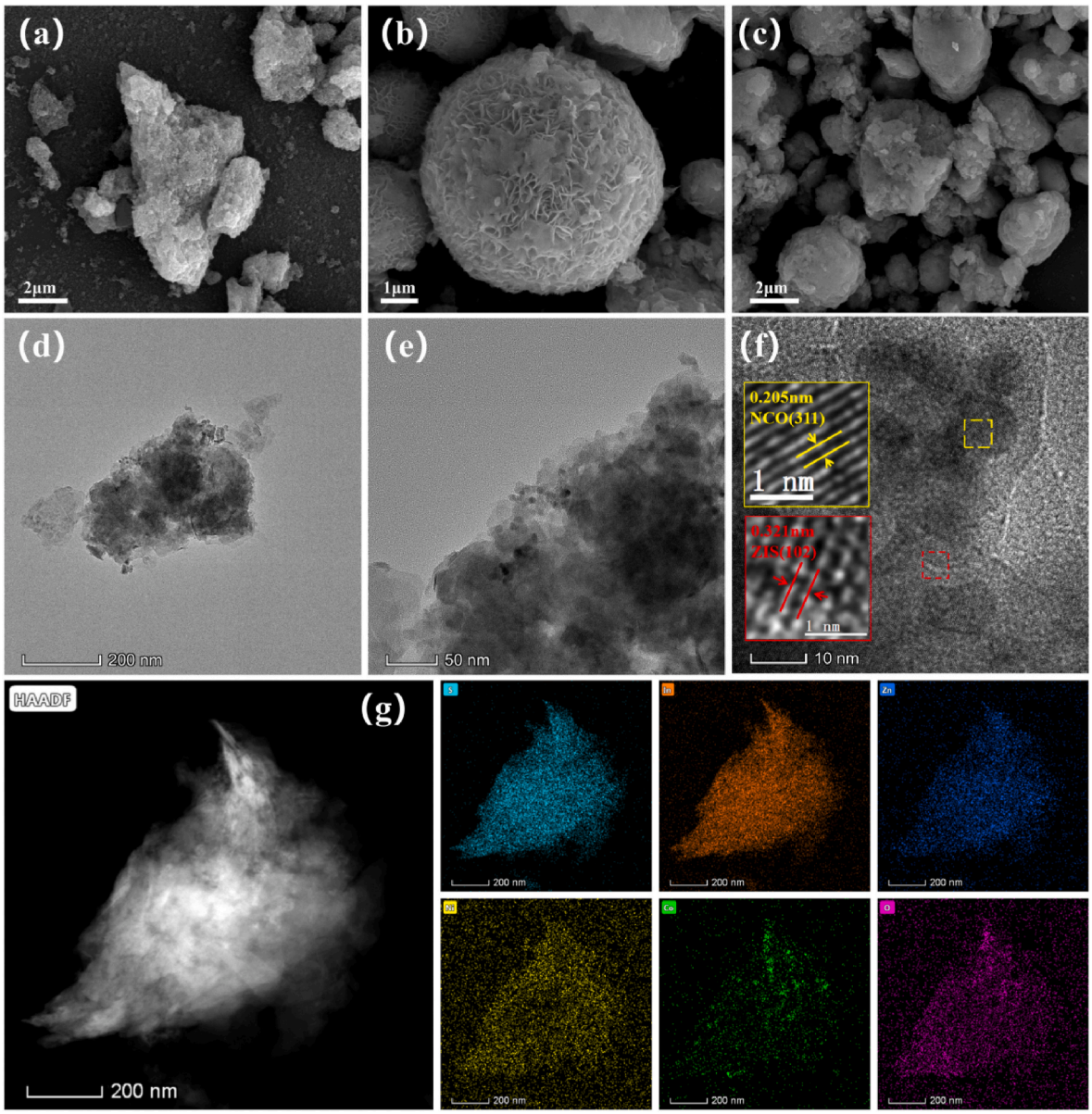

Fig. 3. SEM images of (a) NCO, (b) ZIS, (c) ZIS/NCO, (d–f) TEM images of ZIS/NCO, (g) TEM-EDS elemental maps of ZIS/NCO.

eV and 873.89 eV have been explicitly identified as vibration satellite peaks specific to nickel species, which align with the spectral features reported in the literature [4]. The high-resolution spectrum of Co 2p (Fig. 4e) was similarly fitted to six peaks, showing two spin-orbit doublets, Co^{3+}. Additionally, two satellite peaks were observed at 779.97 eV and 795.06 eV, which were attributed to the Co^{3+} signal [41], and at 782.22 eV and 797.32 eV, which were attributed to the Co^{2+} signal. The high-resolution spectrum of O 1s, as illustrated in Fig. 4f, was fitted to two peaks at 531.12 and 529.43 eV. These peaks represent O_{abs} and O_{latt} [42], which correspond to adsorbed and lattice oxygen, respectively. In the ZIS/NCO composite, the binding energies of all elements were modified in comparison to the single catalyst, with S, In, and Zn exhibiting a shift towards high binding energies, while Ni, Co, and O displayed a shift towards low binding energies, indicating a robust interaction between ZIS and NCO.

The photocatalytic activity of the ZIS/NCO series of materials were investigated under visible light conditions using a 300 W xenon lamp as the source of irradiation. Deionized water was employed as the reaction medium, and triethanolamine (TEOA) was used as the sacrificial agent. The outcomes of the photocatalytic performance assessments conducted on all the materials are illustrated in Fig. 5a. The NCO material exhibits minimal hydrogen production activity, whereas the $ZnIn_2S_4$ material demonstrates a hydrogen production rate of 1149 μmol h^{-1} g^{-1}. The photocatalytic activity of ZIS/NCO is enhanced with the increase of the NCO content. The ZIS/NCO-7 composite exhibits a maximum photocatalytic hydrogen production rate of 4729 μmol h^{-1} g^{-1}, representing a significant 4.11-fold enhancement in comparison to the pure ZIS. Furthermore, we calculated the apparent quantum yields (AQY) of ZIS/NCO-7, ZIS/NCO-5, ZIS, and NCO at 380 nm using established AQY calculation formulas, yielding 2.33 %, 1.36 %, 0.56 %, and 0.056 % respectively. Comparative analysis revealed that the composite material ZIS/NCO-7 exhibited significantly higher AQY values than either individual ZIS or NCO [43]. This enhancement can be attributed to the formation of a unique ZIS/NCO heterostructure, which is the result of a strong interaction between the two components. However, when the mass fraction of NCO was increased to 7 %, the hydrogen production rate of ZIS/NCO-9 decreased to 2380 μmol h^{-1} g^{-1}, and the photocatalytic activity was reduced. This may be attributed to the excess NCO hindering the light absorption of ZIS.

The outcomes of the control experiment utilising ZIS/NCO-7 in the

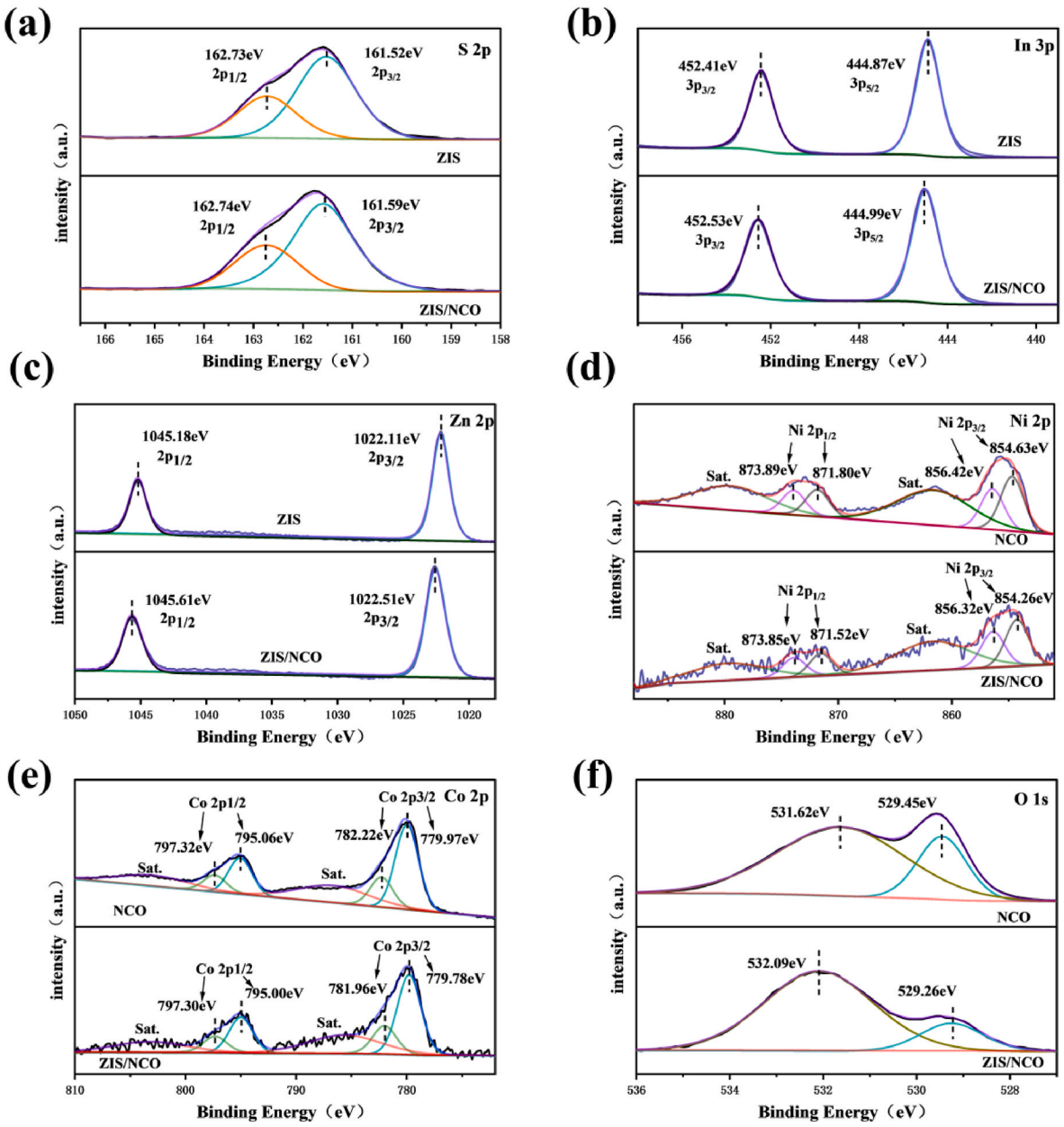

Fig. 4. High-resolution XPS spectra of (a) S 2p, (b) In 3p, (c) Zn 2p, (d) Ni 2p, (e) Co 2p, and (f) O 1s levels of ZIS, NCO, and ZIS/NCO, respectively.

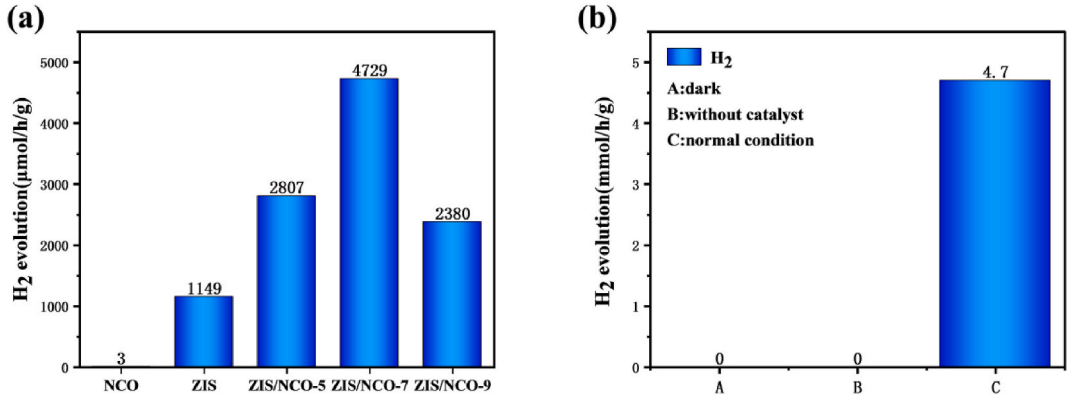

Fig. 5. (a) Comparison of photocatalytic H_2 production rate for different ratios of photocatalysts. (b) Hydrogen evolution rate of ZIS/NCO-7 sample under different conditions.

absence of solar radiation are illustrated in Fig. 5b. The absence of product formation serves to underscore the necessity of sunlight for the production of hydrogen. The absence of a catalyst did not result in the formation of any product, thereby indicating that the production of hydrogen is not a spontaneous process. The experiments demonstrated that sunlight and a catalyst are indispensable for the production of hydrogen from water. Fig. S2 illustrates the sustained hydrogen production performance of ZIS/NCO-7 across four cycles. To verify its resistance to photocorrosion, XRD analyses were conducted after the cycling tests. Fig. S3 shows no significant changes in the XRD patterns before and after the cycles, indicating that the catalyst maintained its structural integrity under the tested cyclic conditions. This suggests that ZIS/NCO-7 exhibits stable performance during repeated photocatalytic processes, without obvious deactivation or structural degradation within the scope of this cyclic experiment.

The considerable influence of photogenerated carrier separation on the photocatalytic hydrogen generation process has been a key focus of recent research [44]. A comprehensive examination of the charge transfer dynamics of these photocatalysts has been undertaken utilising techniques such as electrochemical impedance spectroscopy (EIS), photocurrent transient measurements (I-T), and steady-state fluorescence spectroscopy (PL). The arc radius of the EIS curve can be used as a direct reflection of the interfacial charge transfer resistance. As illustrated in Fig. 6a, the radius of the EIS curve for ZIS/NCO-7 is smaller than that of ZIS and NCO, indicating a reduction in charge transfer resistance and an increase in charge transfer efficiency. This provides further evidence to support the enhanced electron transfer capability of NCO. Fig. 6b illustrates the photocurrent intensity of ZIS, NCO and ZIS/NCO-7 over multiple cycles. In general, a stronger photocurrent indicates a higher efficiency of carrier separation. In the presence of light, the photocurrent intensity of ZIS/NCO-7 composites is greater than that of ZIS and NCO, indicating that the incorporation of NCO markedly enhances the charge separation efficiency of ZIS, which in turn improves its photocatalytic performance.

To gain further insight into the carrier complexation of ZIS and ZIS/NCO composites, photoluminescence (PL) spectroscopic tests were conducted. In general, a lower PL intensity is indicative of a higher charge separation efficiency [45]. The PL results are presented in Fig. 6c. In comparison with ZIS alone, the composite displays a diminished signal, indicating a reduced rate of carrier complexation. In particular, the peak of ZIS/NCO-7 is the most sparse and weak, indicating the highest carrier separation efficiency. This is consistent with the observation that this composite exhibits the best performance in photocatalytic hydrogen production experiments. Furthermore, it provides evidence that the addition of the NCO co-catalyst significantly inhibits carrier complexation.

In order to gain insight into the underlying mechanism of the photocatalytic reaction, the band gap (E_g) and light absorption capabilities of the samples were evaluated through the use of diffuse reflectance spectroscopy (DRS). The intrinsic absorption edge of pure ZIS is approximately 540 nm, whereas NCO exhibits pronounced light absorption within the range of 300–800 nm (Fig. 7a), which may be attributed to the natural background absorption of black NCO. The combination of ZIS and NCO significantly increases the visible light absorption of the composite material compared to ZIS alone. This indicates that the incorporation of NCO markedly enhances the visible light absorption capacity of the material, which is advantageous for utilising solar energy to facilitate hydrogen production. According to the Kubelka-Munk (K-M) equation, the band gap values of NCO and ZIS can be calculated as 2.11 eV and 2.41 eV, respectively (Fig. 7b).

The energy band structures of the photocatalysts were subjected to further investigation through the utilisation of Mott-Schottky

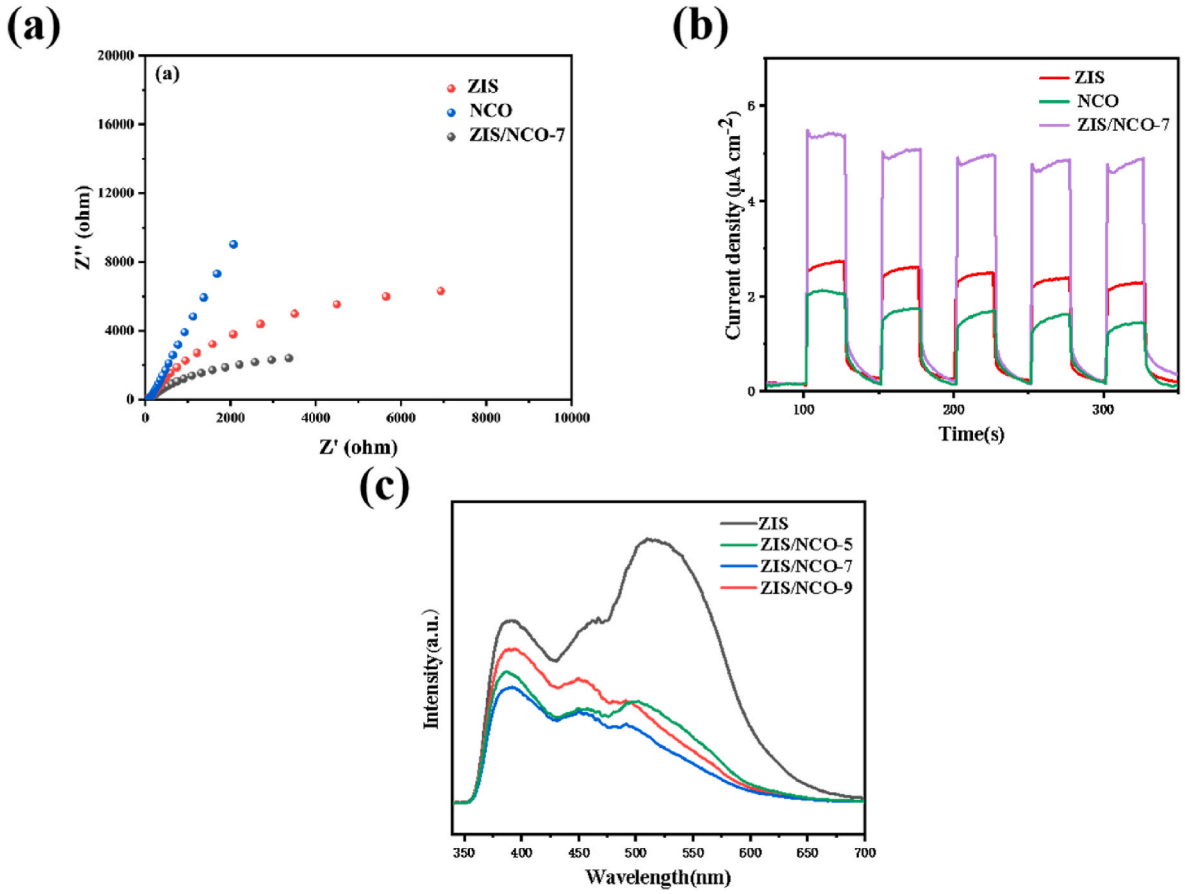

Fig. 6. (a) EIS Nyquist plots; (b) photocurrent mapping under a 300 W Xe-lamp with a cutoff filter (380 nm); (c) PL spectra.

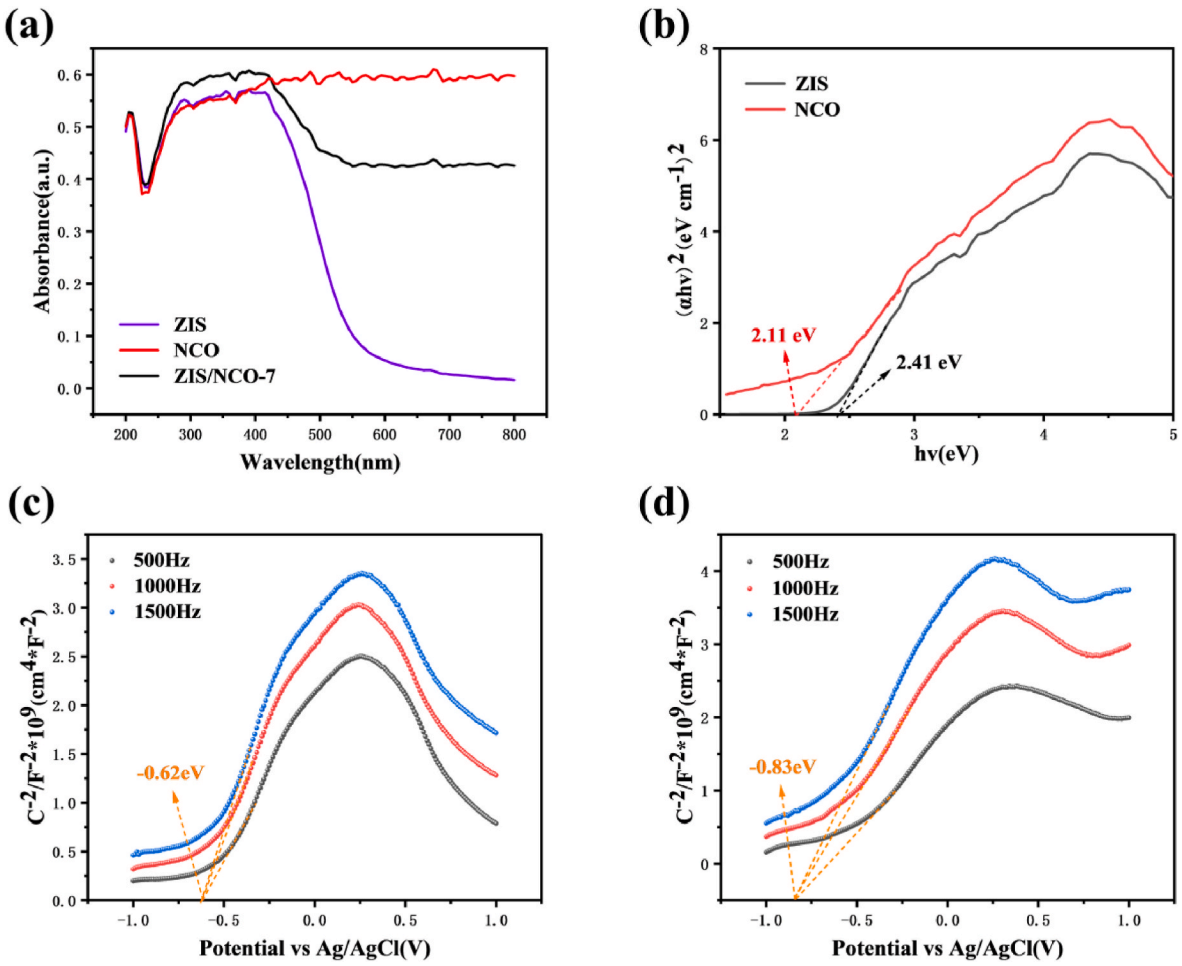

Fig. 7. (a) UV–vis diffuse reflectance spectra of ZIS, NCO, and ZIS/NCO; (b) Band gap energy for ZIS and NCO; (c–d) Mott-Schottky plots for ZIS and NCO.

experiments. Fig. 7c and d demonstrate that NCO and ZIS exhibit positive slopes, thereby confirming that they are both n-type semiconductors [39]. The flat-band potentials (E_{fb}) of NCO and ZIS are −0.62 eV and −0.83 eV (with respect to Ag/AgCl) and −0.42 and −0.63 eV with respect to NHE ($E_{NHE} = E_{Ag/AgCl} + 0.197$), respectively. In the literature, it has previously been noted that the conduction band bottom (CB) is roughly equivalent to the flat band potential for n-type semiconductors. Therefore, the conduction band bottoms of NCO and ZIS are approximately −0.42 eV and −0.63 eV (with respect to NHE), respectively. From the equation $E_g = E_{VB} - E_{CB}$, the top of the valence band (E_{VB}) is approximately 1.69 eV and 1.78 eV for NCO and ZIS, respectively.

To gain deeper insight into the charge transfer mechanism within ZIS/NCO heterojunctions, electron paramagnetic resonance (EPR) spectroscopy was employed to analyze the charge migration process. Using 5,5-dimethyl-1-pyrroline-*n*-oxide (DMPO) as a spin-trapping agent, the catalysts were examined under visible light exposure. The EPR spectra revealed distinct DMPO-·O_2^- signals in both pristine ZIS and ZIS/NCO samples, with the signal intensity being significantly higher in pure ZIS than in the composite material. Notably, no detectable DMPO-·O_2^- signal was observed in pure NCO samples (Fig. 8). These results indicate that ZIS exhibits a greater capacity for generating Cd_2O_2 radicals than NCO, while simultaneously demonstrating electron transfer from the conduction band of ZIS to that of NCO.

Based on these analyses, the potential charge transfer pathways of type I heterojunction are proposed. As shown in Fig. 9, under visible light irradiation, the VB electrons of ZIS are excited and jumped to the CB, and since the conduction band energy level of ZIS is higher than that of NCO, the electrons in the conduction band of ZIS are transferred to

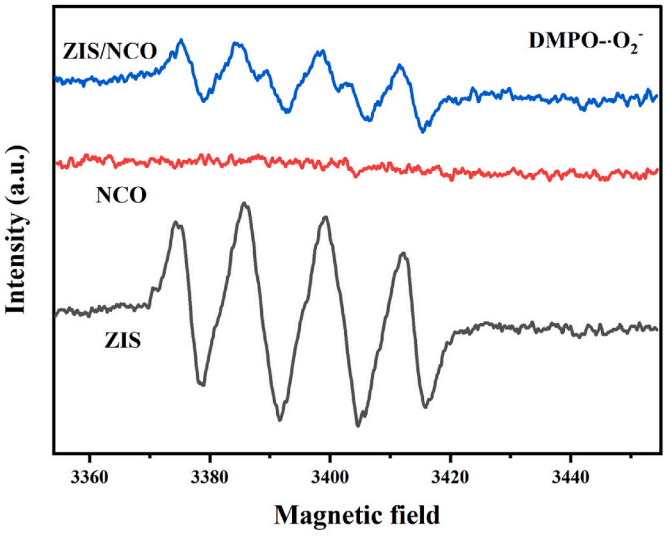

Fig. 8. Electrical paramagnetic resonance (EPR) spectra of DMPO-·O_2^-

NCO when they come into contact with each other, leading to the reduction reaction of H^+ in the water and the production of H_2. Since ZIS and NCO are n-type semiconductors, the difference in the mobility of electrons and holes is a critical factor. Since both ZIS and NCO are n-type semiconductors, the difference in mobility between electrons and holes is a critical factor. Since the mobility of holes in semiconductors is lower

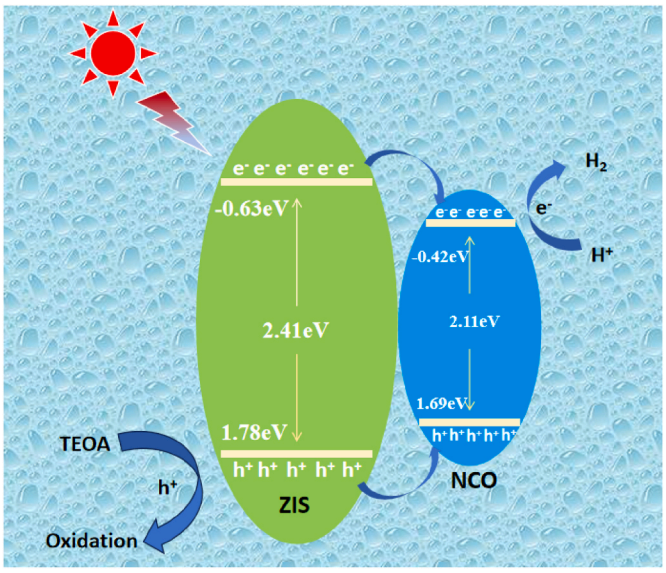

Fig. 9. The proposed charge transfer mechanism.

than that of electrons, the holes in the ZIS valence band are destined to be utilized by sacrificial carriers. This mechanism plays a key role in efficiently separating electrons and holes to improve the photocatalytic efficiency.

4. conclusion

In this work, the preparation of ZIS/NCO heterojunction catalysts was successfully achieved through a straightforward mechanical stirring method. The incorporation of NCO markedly enhanced the photocatalytic performance and stability of ZIS catalysts. Upon reaching a mass fraction of 7 % NCO, the composite catalyst exhibited a peak photocatalytic hydrogen production rate of 4.7 μmol h^{-1} g^{-1}, representing a 4.11-fold increase compared to the pure ZIS catalyst. Following four hydrogen production cycles, the photocatalytic hydrogen production efficiency of the composite catalyst remained stable, exhibiting minimal decline. Furthermore, given that the conduction band position of ZIS is higher than that of NCO, photoexcited electrons are spontaneously migrated to the surface of NCO. In contrast, the migration rate of holes is considerably lower than that of electrons in n-type semiconductors, which facilitates the effective separation of photogenerated electrons and holes at the ZIS/NCO interface, thereby enhancing the performance and stability of the catalyst. It can therefore be concluded that the ZIS/NCO heterojunction has significant potential for use in photocatalytic hydrogen production.

CRediT authorship contribution statement

Xulong Sun: Writing – original draft, Data curation. **Yongping Luo:** Data curation. **Yong Chen:** Data curation. **Yuhua Dai:** Formal analysis. **Yu Xie:** Funding acquisition. **Yuxiu Wang:** Writing – review & editing, Funding acquisition. **Jiansheng Zhang:** Project administration.

Declaration of competing interest

The authors declare that they have no known competing financial interests or personal relationships that could have appeared to influence the work reported in this paper.

Acknowledgements

This work was financially supported by the National Natural Science Foundation of China (No. 22066017, 22362027, 22462033), High-level Scientific Research and Innovation Team of Yuzhang Normal University, China (YZTD202301) and Jiangxi Province, China “double thousand plan” project.

Appendix A. Supplementary data

Supplementary data to this article can be found online at https://doi.org/10.1016/j.ijhydene.2025.151031.

References

[1] Vasseghian Y, Joo SW, Choo J, et al. Photocatalytic materials for solar-driven hydrogen generation. Curr Opin Chem Eng 2024;46:101055.
[2] Pan Y, Lin B, Li X, et al. Porous hierarchical sphere g-C_3N_4 with coordinated Co-ions as an efficient and stable self-Fenton photocatalyst for the removal of antibiotic. Sep Purif Technol 2025;354:129456.
[3] Li R, Luan J, Zhang Y, et al. A review of efficient photocatalytic water splitting for hydrogen production. Renew Sustain Energy Rev 2024;206:114863.
[4] Li B, Ning C, Pan Y, et al. In-situ MOF-derived hierarchical Ni-In_2S_3 tube for efficient photocatalytic production of H_2O_2 with simultaneous degradation of ciprofloxacin. J Environ Chem Eng 2025;13(1):115301.
[5] Yuan C, Shen Y, Zhu C, et al. Ru single-atom decorated black TiO_2 nanosheets for efficient solar-driven hydrogen production. ACS Sustainable Chem Eng 2022;10 (31):10311–7.
[6] Sun K, Liu M, Pei J, et al. Incorporating transition-metal phosphides into metal-organic frameworks for enhanced photocatalysis. Angew Chem 2020;132(50): 22937–43.
[7] Fang Juan, Fan Sun, Amanj Kheradmand, et al. Solar thermo-photo catalytic hydrogen production from water with non-metal carbon nitrides. Fuel 2023;353: 129277.
[8] Sambyal S, Sharma R, Mandyal P, et al. Advancement in two-dimensional carbonaceous nanomaterials for photocatalytic water detoxification and energy conversion. J Environ Chem Eng 2023;11(2):109517.
[9] Liu X, Liu Y, Dong S, et al. Turning trash into treasure: recycling $Ti_3C_2T_x$ oxide through channel engineering towards high-capacity supercapacitors[J]. Available at: SSRN 4367786.
[10] Chinnasamy C, Perumal N, Choubey A, et al. Recent advancements in MXene-based nanocomposites as photocatalysts for hazardous pollutant degradation-A review. Environ Res 2023:116459.
[11] Kang E, Kim JH. Highly boosted photocatalytic H_2 production from ZnS particles assisted by Cd-Cu co-doping. J Environ Chem Eng 2023;11(3):109833.
[12] Ruziwa DT, Oluwalana AE, Mupa M, et al. Pharmaceuticals in wastewater and their photocatalytic degradation using nano-enabled photocatalysts. J Water Proc Eng 2023;54:103880.
[13] Wang X, Shao Y, Pan J, et al. Exploring the green technique based on photocatalysis to produce hydrogen peroxide: progress and challenge. Chem Eng J 2024:151923.
[14] Chen L, Zhao J, Li J, Zhuang Y, Guo D, Meng S, Zhang D, Yang X, Sui G. Cu/Zn-bimetallic organic framework-derived RGO/CuO-ZnO Z-scheme heterojunction for efficient photocatalytic hydrogen production. Int J Hydrogen Energy 2025;103: 45–52.
[15] Xiao Y, Tian J, Miao H, et al. Efficient photocatalytic H_2 evolution over $CuCo_2S_4$ decorated $ZnIn_2S_4$ with S-scheme charge separation way. Int J Hydrogen Energy 2024;88:441–9.
[16] He G, Wang J, Lv X, et al. Exploring the photothermal effect in the photocatalytic water splitting over Type II $ZnIn_2S_4/CoFe_2S_4$ composites. J Colloid Interface Sci 2024.
[17] Yi L, Nkinahamira F, Jiang H, et al. Mo_2N decorated hierarchical $ZnIn_2S_4$ with sulfur-rich vacancy photocatalyst for efficient photocatalytic hydrogen production. J Environ Chem Eng 2023;11(3):110240.
[18] Zeng Y, Liu S, Zhu G, et al. In-situ self-assembled flower-like $ZnIn_2S_4/CdIn_2S_4$ composites with enhanced interfacial charge transfer and photocatalytic degradation of atrazine. J Clean Prod 2023;429:139617.
[19] Huang F, Li Z, Xu Y, et al. Excellent anti-photocorrosion and hydrogen evolution activity of $ZnIn_2S_4$-based photocatalysts: In-situ design of photogenerated charge dynamics. Chem Eng J 2023;473:145430.
[20] Wan J, Liu L, Wu Y, et al. Exploring the polarization photocatalysis of $ZnIn_2S_4$ material toward hydrogen evolution by integrating cascade electric fields with hole transfer vehicle. Adv Funct Mater 2022;32(35):2203252.
[21] Matsuoka H, Higashi M, Nakada A, et al. Enhanced H_2 evolution on $ZnIn_2S_4$ photocatalyst under visible light by surface modification with metal cyanoferrates. Chem Lett 2018;47(7):941–4.
[22] Wang Y, Ye J, Hu B, et al. NiO co-catalyst modification $ZnIn_2S_4$ driving efficient hydrogen generation under visible light. Sep Purif Technol 2023;320:124096.
[23] Fan Y, Tian F, Yang R, et al. Effects of hydrothermal time on the properties, morphology and photocatalytic activity of rose-like microspheres $ZnIn_2S_4$. ChemistrySelect 2019;4(46):13663–7.
[24] Li T, Tsubaki N, Jin Z. S-scheme heterojunction in photocatalytic hydrogen production. J Mater Sci Technol 2024;169:82–104.

[25] Sun B, Zhou W, Li H, et al. Synthesis of particulate hierarchical tandem heterojunctions toward optimized photocatalytic hydrogen production. Adv Mater 2018;30(43):1804282.
[26] Qiao F, Liu W, Yang J, et al. Fabrication of ZnO/$CuInS_2$ heterojunction for boosting photocatalytic hydrogen production. Int J Hydrogen Energy 2024;53:840–7.
[27] Ren S, Wang S, Chen H, et al. S vacancies engineering $ZnIn_2S_4$ nanosheets for boosted photocatalytic hydrogen evolution. Int J Hydrogen Energy 2024;51:1128–35.
[28] Liang S, Sui G, Guo D, Luo Z, Xu R, Yao H, Li J, Wang C. g-C_3N_4-wrapped nickel doped zinc oxide/carbon core-double shell microspheres for high-performance photocatalytic hydrogen production. J Colloid Interface Sci 2023;635:83–93.
[29] Song J, Li J, Zhuang Y, Guo D, Meng S, Zhang D, Yang X, Li Y, Sui G. Grain boundary engineering-assisted Cu in-situ doped ZnS/ZnCdS heterojunction for boosting photocatalytic hydrogen evolution. Sep Purif Technol 2025;367:132889.
[30] Yue Y, Sui G, Zhuang Y, Guo D, Meng S, Zhang D, Yang X, Liu N, Li Y, Li J. In situ doping and vacancy strategy trigger rapid charge transport of Cu/S-$In(OH)_3$ for boosting photocatalytic hydrogen production. Sep Purif Technol 2025;369:133018.
[31] Ren M, Li J, Guo D, Zhang D, Zhuang Y, Meng S, Li X, Yang X, Sui G. Lattice coherency engineering trigger rapid charge transport at the heterointerface of Te/In_2O_3@MXene photocatalysts for boosting photocatalytic hydrogen evolution. J Colloid Interface Sci 2025;685:733–42.
[32] Yang S, Wang K, Wu Z, et al. Probing charge transfer of $NiCo_2O_4$/g-C_3N_4 photocatalyst for hydrogen production. J Mater Sci Technol 2024;200:253–64.
[33] Wang B, Si Y, Du M, et al. Broad-spectrum response of $NiCo_2O_4$-$ZnIn_2S_4$ p-n junction synergizing photothermal and photocatalytic effects for efficient H_2 evolution. Catal Sci Technol 2024;14(16):4646–54.
[34] Tang Y, Zhang D, Qiu X, et al. Fabrication of a $NiCo_2O_4/Zn_{0.1}Cd_{0.9}S$ pn heterojunction photocatalyst with improved separation of charge carriers for highly efficient visible light photocatalytic H_2 evolution. J Alloys Compd 2019;809:151855.
[35] Ma X, Hou S, Li D, et al. Novel noble-metal-free $NiCo_2O_4/CdIn_2S_4$ S-scheme heterojunction photocatalyst with redox center for highly efficient photocatalytic H_2 evolution. Appl Surf Sci 2024;672:160895.
[36] Wang Y, Li X, Zhao R, et al. High-performance photocatalysis afforded by g-C_3N_4/$NiCo_2O_4$-decorated carbon cloth. Appl Surf Sci 2020;532:147410.
[37] Barrios CE, Albiter E, y Jimenez JMG, et al. Photocatalytic hydrogen production over titania modified by gold–Metal (palladium, nickel and cobalt) catalysts. Int J Hydrogen Energy 2016;41(48):23287–300.
[38] Pan J, Li H, Li S, et al. The enhanced photocatalytic hydrogen production of nickel-cobalt bimetals sulfide synergistic modified CdS nanorods with active facets. Renew Energy 2020;156:469–77.
[39] Liu Y, Li M, Geng L, et al. In situ growth of $ZnIn_2S_4$ nanosheets on 2D NiFeS sheets from vulcanization of Ni-Fe LDH for enhancing photocatalytic hydrogen production. Int J Hydrogen Energy 2024;87:476–84.
[40] Jiang J, Wang X, Zhang C, et al. Porous 0D/3D $NiCo_2O_4$/g-C_3N_4 accelerate emerging pollutant degradation in PMS/vis system: degradation mechanism, pathway and toxicity assessment. Chem Eng J 2020;397:125356.
[41] Souza HCD, Sankar A, Sivalingam Y, et al. Boosting interfacial charge transfer of 2D g-C_3N_4 by incorporating 0D Ag and 2D metallic $NiCo_2O_4$ as dual electron donor and acceptor co-catalysts for photocatalytic hydrogen evolution. Int J Hydrogen Energy 2024;94:433–43.
[42] Su P, Liu H, Jin Z. Metal organic framework-derived $Co_3O_4/NiCo_2O_4$ hollow double-shell polyhedrons for effective photocatalytic hydrogen generation. Appl Surf Sci 2022;571:151288.
[43] Liang S, Sui G, Li J, Guo D, Luo Z, Xu R, Yao H, Wang C, Chen S. ZIF-L-derived porous C-doped ZnO/CdS graded nanorods with Z-scheme heterojunctions for enhanced photocatalytic hydrogen evolution. Int J Hydrogen Energy 2022;47(21):11190–202.
[44] Shi H, Yan B, Xu H, et al. $NiCS_3$: a cocatalyst surpassing Pt for photocatalytic hydrogen production. J Colloid Interface Sci 2024;659:878–85.
[45] Saddique Z, Imran M, Javaid A, et al. Bismuth-based nanomaterials-assisted photocatalytic water splitting for sustainable hydrogen production. Int J Hydrogen Energy 2024;52:594–611.